Geophysical Research Letters

Supporting Information for

Marine Ice Cliff Instability Mitigated by Slow Removal of Ice Shelves

Fiona Clerc[1], Brent M. Minchew[2], Mark D. Behn[3]

[1]MIT-WHOI Joint Program in Oceanography/Applied Ocean Science & Engineering, Cambridge MA

[2]Department of Earth, Atmospheric and Planetary Sciences, Massachusetts Institute of Technology, Cambridge MA

[3]Department of Earth and Environmental Sciences, Boston College, Chestnut Hill MA

Contents of this file

Text S1 to S2

Figures S1 to S4

Additional Supporting Information (Files uploaded separately)

Caption for Movie S1

Text S1. Methods

S1.1 Failure modes

We assume a tensile brittle-ductile strain rate of 4×10^{-7} 1/s (dashed red line, **Figure 1a**), constrained experimentally and scaled to a Glen's flow law parameter of A = 10^{25} s^{-1} Pa^{-3} and grain size of d ~ 1 mm (Schulson & Duval, 2009). Uncertainties in the tensile brittle-ductile strain rate associated with the prescribed material properties of ice affect our critical height estimates. We explore these effects in Figure 4, Section 4 of the main text, Figure S4, and Section 2.5 of the supplement.

Previous parametrizations of cliff failure which presume failure involves Coulombic faulting (Bassis & Walker, 2012; DeConto & Pollard, 2016) are characterized by the Mohr-Coulomb failure criterion, and depend on the assumed coefficient of internal friction (μ). Bassis and Walker (2012) use $\mu = 0$ to obtain a constant yield stress of τ_{yield} = 1 MPa, equal to the cohesion of ice. This assumption follows from the observed lack of tall marine-terminating ice cliffs supported by shallow water depths. Within the context of buttressing ice shelf removal over finite timescales, glacier termini represent the static end-member case; previously tall cliffs may have deformed viscously to reach flotation (hence the dearth of observation of such cliffs). Additionally, the material properties (i.e., coefficient of internal friction and tensile strength) of intact ice are different from the damaged ice found at glacier termini, motivating our choice of a non-zero coefficient of friction. The coefficient of kinetic friction observed from sliding ice blocks against each other may range from 0.15 to 0.76 and depend on both temperature and sliding velocity (Schulson & Fortt, 2012). We use an intermediate value of $\mu = 0.5$. While this value is poorly constrained, our conclusion that the Tensile regime controls the initiation of cliff failure (instead of the Thermal Softening or Coulombic regimes) means varying μ would not affect our results.

S1.2 Rheology and material properties

We assume ice is incompressible and adopt a Maxwell viscoelastic rheology for ice, described by the constitutive relation relating the deviatoric stress (τ_{ij}) and strain-rate ($\dot{\epsilon}_{ij}$) tensors (Eq. 1).

$$\dot{\epsilon}_{ij} = \frac{1}{2G}\dot{\tau}_{ij} + A\tau_e^{n-1}\tau_{ij} \tag{1}$$

Here τ_e is the effective deviatoric stress (the square root of the second invariant of the deviatoric stress tensor). We can calculate the effective strain rates from the deviatoric stresses and the stressing rate, which is set by the transition time Δt ($\dot{\tau}_{ij} \approx \Delta\tau_{ij}/\Delta t$). Using a shear modulus G = 2 GPa, we approximate the rheology of a Burgers viscoelastic material with a shear modulus of 3.8 GPa. While the Burgers element better models the viscoelastic rheology of ice, the Maxwell model is a valid approximation over timescales (Δt) longer than 0.04 days (Gudmundsson, 2011). We set the Glen law pre-exponential parameter to $A = 1.2\times10^{-25}$ s^{-1} Pa^{-3} (corresponding to a temperature T = -20ºC; Cuffey & Paterson, 2010). We consider cases with both Newtonian and non-Newtonian rheologies. For the non-Newtonian case, we set the stress exponent n=3. For the Newtonian case, we prescribe an average effective deviatoric stress (τ_e) to obtain a constant effective viscosity ($\eta_{eff} = [2A\,(\tau_e^{ave})^{n-1}]^{-1}$). With these approximations and assumptions, the constitutive relation becomes:

$$\dot{\epsilon}_{ij} \approx \frac{1}{2G}\frac{\Delta\tau_{ij}}{\Delta t} + A\tau_e^{n-1}\tau_{ij} = \frac{1}{2\eta_{eff}}\left[\left(\frac{t_R}{\Delta t}\right)\Delta\tau_{ij} + \tau_{ij}\right] \tag{2}$$

If we assume an effective deviatoric stress of 220 kPa (the average stress τ_e^{ave} for a sub-aerial cliff height of 100 m), we obtain an effective viscosity of $\eta_{eff} = 9\times10^{13}$ Pa·s. The effective viscosity scales with the subaerial cliff height. We assume temperature is constant throughout the ice cliff, and test values of A corresponding to a range of plausible temperatures from -35 to -3ºC (Cuffey & Paterson, 2010). We set the densities of the ice and water to 900 and 1000 kg/m^3, respectively.

S1.3 Numerical method

We consider two ice geometries in which we either keep the ice thickness (H) constant at 1000 m (**Figures S1 & S2**) or assume the cliff is at flotation such that the total ice thickness (H) and water depth (D) increase with the subaerial cliff height (h) (**Figures 3 & S3; Movie S1**). The horizontal domain size is 3000 m. Numerical tests show that increasing this horizontal distance does not affect stresses and strain rates in the zone of interest (within 500 m of the cliff face), thus excluding edge effects near the left boundary. We impose a no-slip boundary condition on the left boundary (where the ice cliff is attached to the remainder of the ice sheet). We impose a free-slip boundary condition on the bottom of the ice block. Over the length of each transition we run 50 timesteps, set the vertical grid size by dividing the subaerial cliff height by 50, and use a horizontal grid size of 20 m.

To simulate deformation we use the model SiStER (Simple Stokes solver for Exotic Rheologies; Olive et al., 2016), a particle-in-cell staggered grid finite difference code that solves the momentum and continuity equations for the velocity and pressure fields. We use the stresses and strain rates from the model runs to determine if and where the ice reaches our failure criteria within each of the deformation regimes shown in **Figure 1a**. We emphasize that our models examine only the viscoelastic deformation leading up to the (inferred) onset of plastic failure; future work is required to simulate deformation after plastic failure.

In the numerical model, we retain the geometry of the analytical solution (**Figure 1b,c**). We set up the ice cliff on the left-hand side of the domain, with a total ice thickness H. On the right-hand side, we initially mirror the ice cliff to simulate the buttressing ice shelf. The "shelf" is thinned linearly to an air/water interface, over a transition time (Δ t), and is replaced by water beneath the shelf and by air above it. At the end of the transition time, the ice shelf is completely replaced by a water layer of height D, and by an air layer exposing a subaerial cliff of height h. The model is run over a range of prescribed subaerial cliff heights (h) and transition times (Δt) over which the buttressing ice shelf is removed.

Text S2. Results

S2.1 Analytical scaling

We derive an analytical scaling from a simplified one-dimensional model of stresses and strain rates along the cliff face. We take the depth (y) as positive downward, where y = 0 at the top of the cliff. We take compressive stresses as negative. We assume the geometry described in the main text (see **Figure 1b,c**).

We first consider the “final” stresses acting on the cliff face once the buttressing ice shelf is fully removed (**Figure 1c**). The final vertical stress arises from the overburden of the ice cliff (of total thickness H):

$$\sigma_{yy}(y) = -\rho_i g y \tag{3}$$

The final horizontal stress arises from the hydrostatic pressure of the water (extending from sea-level at y = h to the ground at y = H):

$$\sigma_{xx}(y) = \begin{cases} 0, & 0 < y \leq h \\ -\rho_w g(y-h), & h < y < H \end{cases} \tag{4}$$

We assume there are no additional stresses present (as the basal boundary condition is free-slip), meaning the vertical stress (σ_{yy}) is the most compressive (σ_1) and the horizontal stress (σ_{xx}) is the least compressive (σ_3). The confinement ratio ($R = \sigma_3/\sigma_1$) gives the local mode of deformation, which is Tensile in the sub-aerial portion of the cliff (y < h) as there $\sigma_3 = \sigma_{xx} = 0$. We also determine the final vertical deviatoric stress:

$$\begin{aligned} \tau_{yy}(y) &= \frac{\sigma_{yy}(y) - \sigma_{xx}(y)}{2} \\ &= \begin{cases} -\frac{1}{2}\rho_i g y, & 0 < y \leq h \\ -\frac{1}{2}\left[\rho_i g y - \rho_w g(y-h)\right], & h < y < H \end{cases} \end{aligned} \tag{5}$$

As we assume the cliff is initially fully buttressed by an ice shelf, the initial deviatoric stress is zero, and the rate of change of the deviatoric stress is approximately the final deviatoric stress divided by the ice-shelf removal time:

$$\dot{\tau}_{yy} \approx \frac{\Delta\tau_{yy}}{\Delta t} \approx \frac{\tau_{yy}}{\Delta t} \tag{6}$$

We determine effective strain rates from deviatoric stresses, assuming a linear Maxwell rheology (Eq. 2). We evaluate the strain rates at sea-level (y = h), where the cliff is most likely to fail, as the local strain rate is maximized and the mode of deformation is in the weak Tensile regime.

$$\begin{aligned}\dot{\epsilon}_e\Big|_{y=h} = ||\dot{\epsilon}_{yy}||\Big|_{y=h} &= \frac{1}{2G}||\dot{\tau}_{yy}||\Big|_{y=h} + A(\tau_e^{ave})^{n-1}||\tau_{yy}||\Big|_{y=h} \\ &= \frac{\rho_i g h}{2}\left[\frac{1}{2G\Delta t} + A(\tau_e^{ave})^{n-1}\right]\end{aligned} \qquad (7)$$

Here τ_e^{ave} is the depth-averaged effective stress and determines the effective viscosity (see section 1.2).

$$\begin{aligned}\tau_e^{ave} &= \frac{1}{H}\int_0^H ||\tau_{yy}||dy \\ &= \frac{1}{H}\left[\int_0^h \frac{1}{2}\big[\rho_i g y\big]dy + \int_h^H \frac{1}{2}\big[\rho_i g y - \rho_w g(y-h)\big]dy\right] \\ &= \frac{g}{4}\left[(\rho_i - \rho_w)H + \rho_w h\big(2 - \frac{h}{H}\big)\right]\end{aligned} \qquad (8)$$

We find the critical height (h^*) above which tensile fractures initiate (green lines in **Figure 4**) by equating the tensile brittle-ductile strain rate to the local deviatoric strain rate. To determine the tensile brittle-ductile strain rate ($\dot{\epsilon}_{BDT}^{tens}$) we employ the parametrization of Schulson and Duval (2009), which depends on the fracture toughness (K_{Ic}), the grain size (d), the ratio of the crack length to the grain size ($\lambda = 3.7$; Lee & Schulson, 1988), and Glen's flow-law parameter.

$$\begin{aligned}&\dot{\epsilon}_{BDT}^{tens} = \dot{\epsilon}_e\Big|_{y=h^*} \\ &\frac{AK_{Ic}^n}{(\lambda d)^{n/2}} = \frac{\rho_i g h^*}{2}\left\{\frac{1}{2G\Delta t} + A\left[\frac{g}{4}\left[(\rho_i - \rho_w)H + \rho_w h^*\big(2 - \frac{h^*}{H}\big)\right]\right]^{n-1}\right\}\end{aligned} \qquad (9)$$

In the viscous limit, $\Delta t \gg t_R$, the elastic term disappears and we obtain a critical height independent of the transition time or flow-law parameter:

$$\frac{K_{Ic}^{n}}{(\lambda d)^{n/2}} = \frac{\rho_i g h^*}{2}\left\{\left[\frac{g}{4}\left[(\rho_i - \rho_w)H + \rho_w h^*\left(2 - \frac{h^*}{H}\right)\right]\right]^{n-1}\right\} \tag{10}$$

S2.2 Numerical simulations

We find that throughout the ice cliff, effective strain rates increase over the length of the transition time (Δt) and are greatest at the end of the transition (this timestep is shown in **Figure 3**). Strain rates are generally greatest near the cliff face, at sea-level (**Figure 3**; top row). The entire cliff is pulled horizontally into the ocean as the buttressing ice shelf is removed, deviatoric stresses are horizontally tensile. Regions of the cliff at subaerial heights are under net tension ($R<0.01$, green in **Figure 3**; middle row), while regions near sea-level are under low confinement corresponding to the Coulombic failure regime (grayscale in **Figure 3**; middle row). For a coefficient of friction $\mu = 0.5$, the Thermal Softening regime dominates much of the submarine ice cliff (purple in **Figure 3**; middle row).

By mapping the modes of deformation onto the ice cliff, we can determine the associated critical strain rate for each region (red lines in **Figure 1a**) and subtract this value from the local strain rate (**Figure 3**; bottom row). We predict failure initiates in regions where this difference is positive (orange). As the tensile brittle-ductile strain rate is much lower than either the compressive brittle-ductile strain rate necessary for Coulombic faulting or the thermal softening critical strain rate, failure always initiates in the unconfined subaerial cliff, near sea-level, in agreement with the analytical prediction.

Consequently, for a given subaerial cliff height, repeating the numerical experiments with different water depths does not change our failure prediction. Similarly, imposing a no-slip basal boundary condition locally increases stresses and strain rates at the base of the cliff, but not enough to overcome the critical strain rate required for large-scale failure within the Thermal Softening deformation regime; our prediction of Tensile failure near sea-level is unaffected (see section S2.5).

For small cliff heights and fast transition times, strain rates are highest closest to the cliff face, suggesting failure initiates with the sloughing off of thin sheets of the subaerial ice. For larger cliff heights, critical strain rates are reached further to the interior of the ice sheet, potentially detaching larger blocks.

Following the onset of Tensile failure, cliffs higher than 540 m undergo plastic deformation. This deformation is potentially dominated by the Thermal Softening deformation mode as the majority of the submarine cliff is under high confinement due to hydrostatic horizontal stresses (purple zone in middle row of **Figure 3**). However, the manner in which these regimes interact and the mode of subsequent deformation remain unclear, and may not necessarily expose the taller cliff faces that would initiate runaway cliff collapse.

S2.3 Evolution of numerical strain rates through time

We further used our numerical models to examine the time-dependent trends of maximum stresses and maximum strain rates within ice cliffs of different subaerial heights and transition times (**Figure S1**). In **Figure S1a,b**, we show the maximum strain rate within regions of the ice cliff undergoing extension (green zone in middle row of

Figure 3), at a given time step. Strain rates are initially near-zero and increase sharply at the onset of the transition period. Strain rates then follow an approximately exponential increase until the supporting cliff is fully removed ($t/\Delta t = 1$). Strain rates are highest at the penultimate timestep ($t/\Delta t = .98$), when a very thin ice shelf presses against the cliff, inducing locally high strain rates. The onset of brittle Tensile failure is predicted when the maximum local strain rate exceeds the tensile brittle-ductile strain rate (red bar, **Figure S1a,b**). Due to their high critical strain rates, we find no scenario in which failure initiates within the Coulombic or Thermal Softening regimes.

For a constant subaerial cliff height (see **Figure S1a** for h=100 m), the effect of changing the transition time depends on whether we are in the viscous or elastic limit of Maxwell viscoelasticity. Within the elastic limit ($\Delta t < 1$ hour or 0.04 days), increasing the transition time leads to a proportional decrease in strain rate. As we run the model with increasing transition times, approaching the viscous limit ($\Delta t > 6$ days), we find strain rates from different runs converge (compare light and dark blue lines in **Figure S1a**) and become independent of the assumed transition time. Moreover, after the end of each transition, all strain rates converge to a final, constant strain rate seemingly controlled by the cliff geometry. Newtonian and non-Newtonian runs behave similarly, especially in the elastic limit where viscosity is negligible. We find the strain rates within a 100-m cliff only reach the tensile brittle-ductile strain rate if the transition time is less than one hour (0.04 days; an order of magnitude less than the Maxwell relaxation time, $t_R \sim 0.6$ days). Effective deviatoric stresses increase steadily through time and are independent of the transition time (**Figure S1c**), as these stresses are primarily controlled by cliff geometry.

Increasing the subaerial cliff height, while keeping the transition time fixed, will increase strain rates and stresses (**Figure S1b,d**). For $\Delta t = 0.6$ days, the maximum cliff height before the Tensile failure criterion is reached lies between 200 and 500 m. If we were to shorten the transition time, the maximum cliff height (before the onset of tensile fractures) would decrease accordingly. However, if we apply the Mohr-Coulomb failure criterion and assume a yield stress of 1 MPa (red bar in **Figure S1c,d**), any cliff greater than ~300 m would fail regardless of transition time. This again implies that different failure criteria make different predictions regarding the conditions under which failure originates.

Finally, we note that the Newtonian and non-Newtonian runs (compare dashed and solid lines in **Figure S1**) generally agree. Most importantly, the maximum strain rate within a given run (which predicts whether or not the cliff fails) is consistent over a range of cliff heights and transition times. This supports our analytical scaling (which employs a Newtonian rheology) and its implications towards cliff failure in nature, as presented in section 4 of the main text.

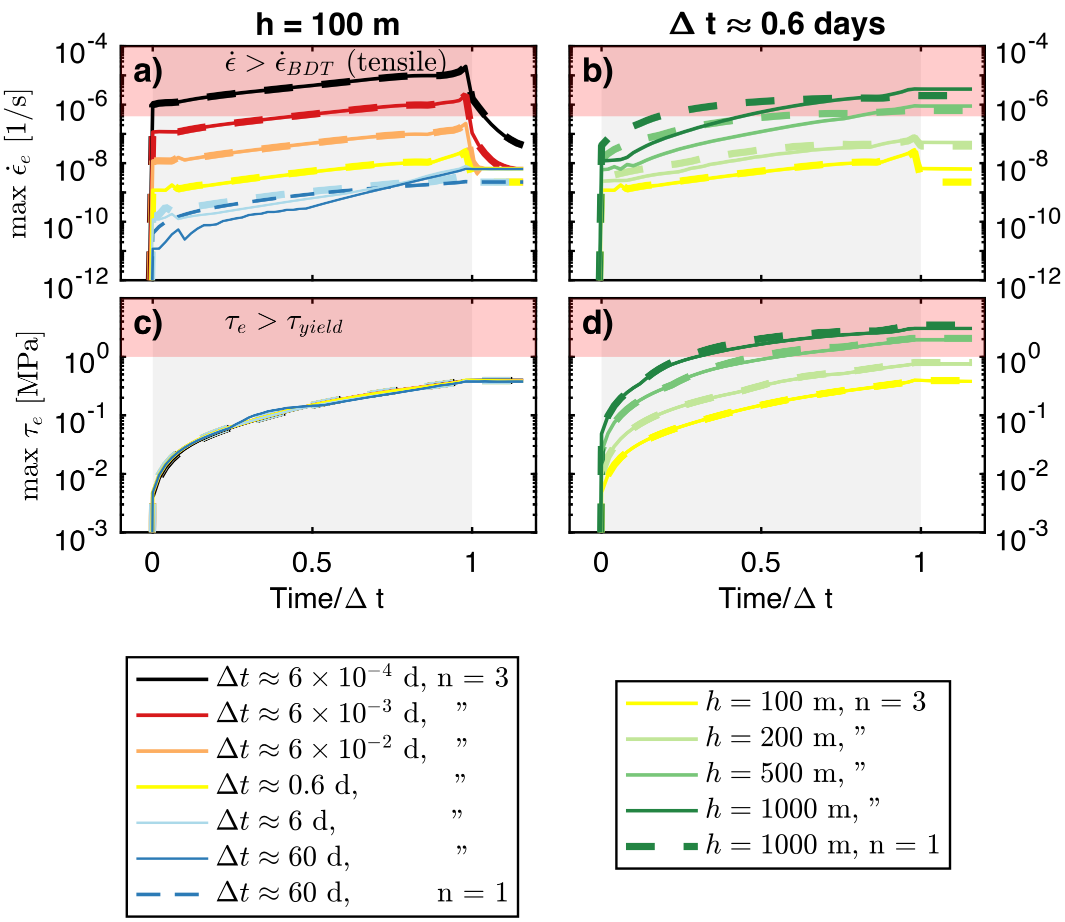

Figure S1*: Evolution through (normalized) time of the maximum strain rates (a,b) and stresses (c,d) within an ice cliff, for different numerical runs. In the left column, the transition time (Δ t) is varied while the subaerial cliff height (h) is fixed at 100 m. In the right column, the cliff height varies while the transition time is fixed at 0.6 days. Both Newtonian runs (dashed lines) and non-Newtonian runs (solid lines) are shown. The top row shows the maximum strain rate within the ice cliff, relative to a critical strain rate; the red bar shows a tensile brittle-ductile strain rate of 4×10^{-7} 1/s. The bottom row shows the maximum effective stress; the red bar shows a yield stress of 1 MPa. The total ice thickness (H) is kept constant at 1000 m (cliffs of subaerial height h = 1000 m are “dry”).*

S2.4 Numerical vs. analytical failure predictions

We next compare the deformation mode calculated by the numerical and analytical models as a function of cliff height and transition time. The maximum strain rates from our numerical runs and our analytical solution predict tensile brittle failure occurs in ice cliffs of similar subaerial height and transition time (**Figure S2a**). Numerical simulations predicting tensile brittle failure (black circles) are characterized by high cliff heights or rapid transition times. Under these conditions, the corresponding analytical strain rate exceeds the tensile brittle-ductile strain rate (red background color in **Figure S2a**). For lower cliff heights and longer transition times, both solutions predict the cliff deforms ductilely (white circles and blue background color in **Figure S2a**). Both models agree the brittle-ductile transition occurs under similar conditions, within the subaerial cliff height/transition time parameter space, with one exception. The numerical run for a 100-m cliff formed over 6×10^{-3} days predicts brittle failure while the analytical solution predicts ductile flow, likely a consequence of the simplifications made in deriving the analytical scaling. The offset between the numerical and analytical strain rates appears systematic (**Figure S2b**). From the numerical runs, 100-m cliffs may be predicted to fail over timescales $\Delta t < 0.02$ days instead of the $\Delta t < 0.003$ days predicted analytically. This timescale remains under an hour and does not change our conclusions. Finally, both approaches indicate deformation is tensile, as their respective maximum strain rates are comparable and follow a similar dependence on transition time (**Figure S2b**) and subaerial cliff height (**Figure S2c**).

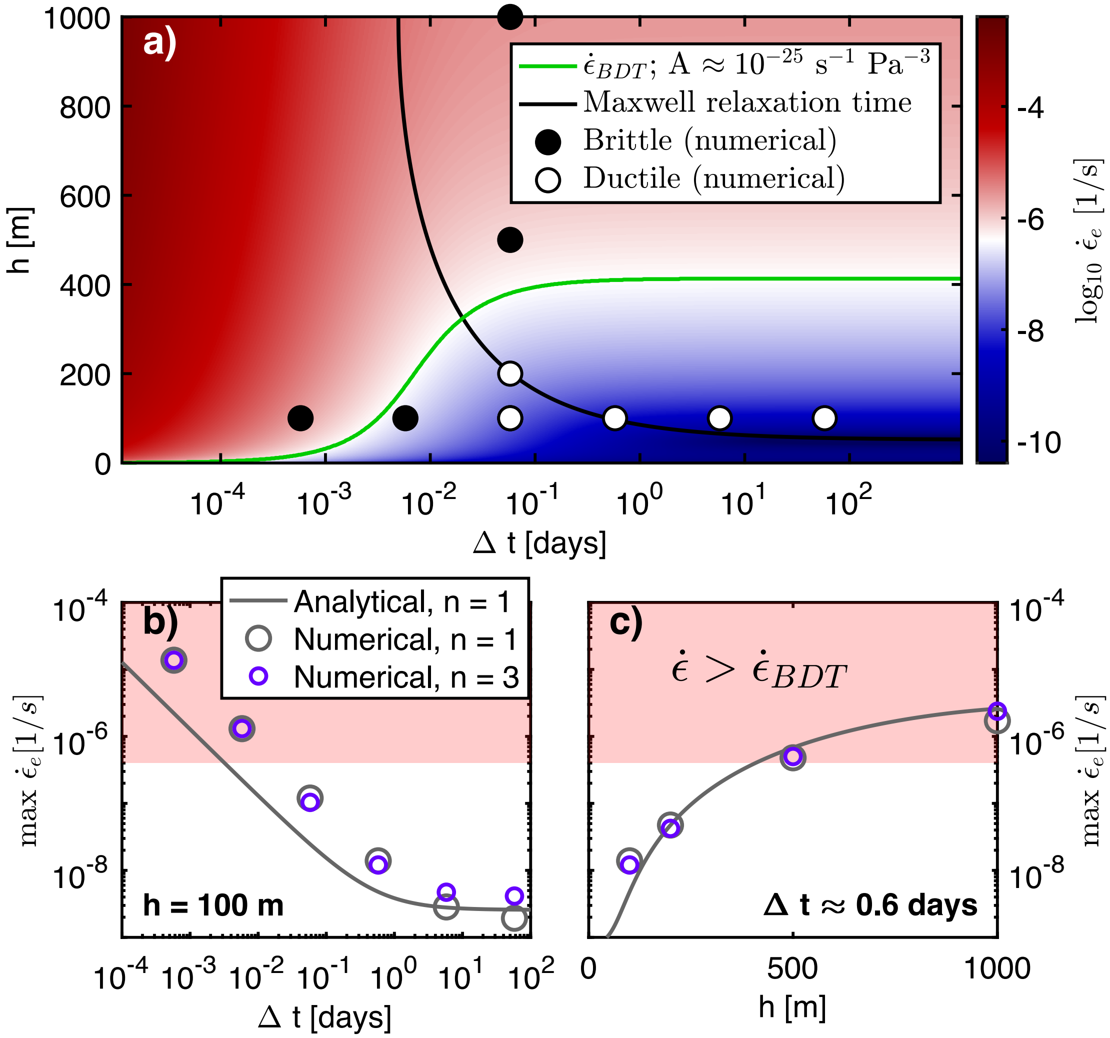

***Figure S2**: a) Analytically derived maximum local strain rates at sea-level (y = h), as a function of sub-aerial cliff height (h) and transition time (Δ t). The total ice thickness (H) is set as 1000 m (instead of at flotation, as in **Figure 4**). The solid green line is the location of the tensile brittle-ductile strain rate (4×10^{-7} 1/s), for $A = 1.2 \times 10^{-25}$ s^{-1} Pa^{-3}. The yellow line is the Maxwell relaxation time. Numerical runs are plotted as circles and are shaded black if any point within the cliff meets the criteria for tensile brittle fracture. b) Comparison of analytically- and numerically-derived maximum strain rates versus* *transition time, through a constant h = 100 m. c) Strain rates versus cliff height, through a constant Δt = 0.6 days.*

S2.5 Comparison with previous studies

We compare our critical cliff height predictions with those made for static cliffs found at glacier termini. The Bassis and Walker (2012) formulation (corrected for a factor of 2 by Ultee and Bassis (2016)) predicts shear failure occurs above a critical height of 440 m for a dry cliff free of pre-existing cracks, and a yield stress of 1 MPa. This height falls within our predicted range (170–710 m). However, we emphasize that while our different solutions make similar predictions concerning the critical cliff height (over long timescales), they represent different physical phenomena (i.e., the initiation of tensile cracks versus Coulombic shear failure). Ma et al. (2017) find that imposing a no-slip basal boundary condition leads to shear failure as described above. However, in our model we find the associated increase in strain rate is localized near the base of the cliff, where high confinement suppresses failure (**Figure S3**). While the strain rate field in **Figure S3** (top row) differs slightly near the base of the cliff compared to the free-slip case (**Figure 3**), the failure predictions (bottom rows) remain essentially the same. Thus, even with a no-slip basal boundary condition, failure is still found to occur higher in the cliff where strain rates are not strongly affected by the basal boundary condition.

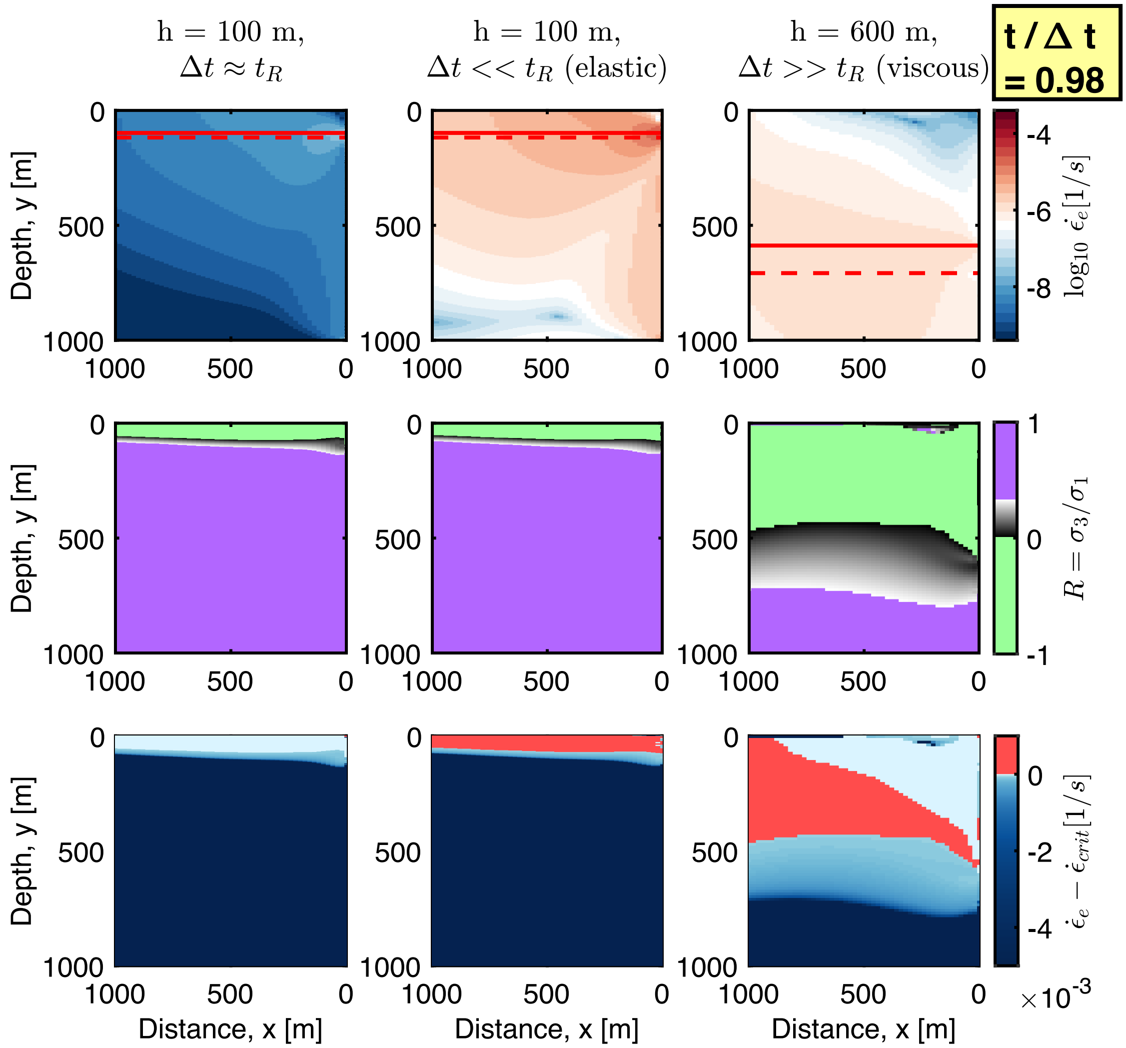

***Figure S3**: Results of numerical simulations for three different ice cliffs at the end of their respective transitions, for a no-slip basal boundary condition (compare to **Figure 3**). From left to right, the cliffs have subaerial heights of 100 m, 100 m, and 600 m, and transition times of 0.6, 6×10^{-4}, and 0.6 days, respectively. The top row shows effective strain rates within the cliff face (the color map is centered around the tensile brittle-ductile strain rate). The middle row shows the confinement ratio (R), color-coded by the 3 deformation regimes: Thermal Softening (purple), Coulombic (gray), or Tensile (green). The bottom row shows the difference between the local strain rates and the* *critical strain rate (defined separately for each deformation regime as in **Figure 1a**). Failure is predicted to initiate in the positive (red) zones.*

Additionally, Parizek et al. (2019) conducted a numerical analysis of a static cliff and applied the Tensile and Coulombic strain rate failure criterion. They conclude that subaerial cliffs higher than ~200 m fail by "slumping", as both the Tensile and Coulombic-faulting criteria are met (using a fracture toughness of 50 kPa $m^{1/2}$ and crack half-length of 50 mm). We reiterate that the initiation of tensile fractures would precede compressive Coulombic failure, changing the strain rate field. Given their choice of parameters, these tensile fractures would initiate in subaerial cliffs higher than 60 m (**Figure S4**). If we were to suspend tensile failure in the viscous limit of our model, using a fracture toughness of 80–120 kPa $m^{1/2}$ and grain sizes of 1–8 mm, we would predict compressive Coulombic failure only occurs in subaerial cliffs higher than 1200 – 5100 m. The discrepancy between our results and those of Parizek et al. (2019) arises largely from their use of a 50 mm characteristic crack half-length (more appropriate for fractured calving fronts), whereas we use crack half-lengths related to the grain size (more appropriate for undamaged ice).

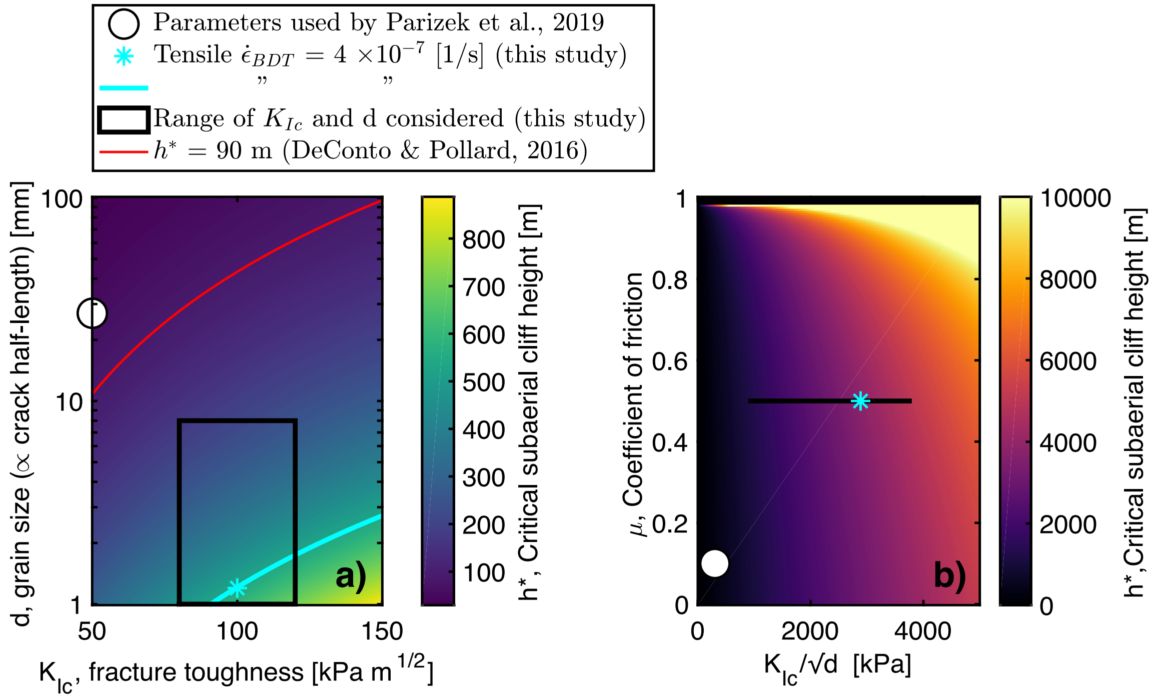

Figure S4*: Critical subaerial cliff heights for the initiation of failure, within space of selected ice material properties. a) Critical cliff height above which strain rates near sea-level exceed the tensile brittle-ductile transition and tensile fractures may initiate, as a function of fracture toughness and crack half-length. b) Critical cliff height above which strain rates near sea-level exceed the compressive brittle-ductile threshold required for the formation of a Coulombic fault.*

Movie S1: *Results of 2-D numerical simulations for three different ice cliffs (as in* ***Figure 3*** *of main text) through time (indicated in top right corner). From left to right, the cliffs have subaerial heights of 100 m, 100 m, and 600 m, and transition times of 0.6,* 6×10^{-4}*, and 0.6 days, respectively. The total ice thickness is set such that the cliff is at flotation (note the 600 m case extends to 6 km and is truncated here) – the grounding line and edge of the cliff is at* $x = 0$*. The top row shows effective strain rates within the cliff face. The color map is centered around the tensile brittle-ductile strain rate of* 4×10^{-7} *1/s (Schulson & Duval, 2009). The red solid and dashed lines show the location of the surface and base of the buttressing ice shelf. The middle row shows the confinement ratio (R), color-coded by the 3 deformation regimes: Thermal Softening (purple), Coulombic (gray), or Tensile (green). The bottom row shows the difference between the local strain rates and the critical strain rate (defined separately for each deformation regime as in* ***Figure 1a****). Failure is predicted to initiate in the positive (red) zone.*